

Chapter 9

Two-Dimensional Terahertz-Infrared-Visible Spectroscopy Elucidates Coupling Between Low- and High-Frequency Modes



Laura Vietze, Mischa Bonn and Maksim Grechko

Abstract Elucidating the interaction between low-frequency modes and other degrees of freedom in soft and hard condensed matter is both scientifically intriguing, technologically important and experimentally challenging. Specifically, revealing the coupling between collective low-frequency and localized high-frequency vibrations in molecules and solids can advance models for energy relaxation and dissipation in such systems, as well as provide new insight into the physical nature of the low-frequency vibrations. The latter is particularly important, since low-frequency vibrations are thermally excited at room temperature and contribute significantly to the thermodynamic properties and functions, such as heat capacity and entropy. To measure the coupling between low- and high-frequency modes, we have developed two-dimensional terahertz-infrared-visible spectroscopy. In this chapter, we describe the experimental approach and theoretical formalism for this new spectroscopy technique and illustrate its application with two examples: liquid water and solid perovskite semiconductors.

9.1 Introduction

Molecular vibrational motions play a pivotal role in condensed phase chemical and biochemical reactions. Because of the quantum nature of molecules, their vibrations can usually occupy only discrete energy levels. The discreteness of the vibrational energy levels is crucial for the role that a given mode plays in molecular dynamics and thermodynamics. Vibrational modes with energy quanta (usually called frequency) comparable to or less than the thermal energy kT are excited at temperature T , in a manner defined by the Boltzmann distribution. Such vibrations constitute thermal fluctuations of a molecular system contributing significantly to its thermodynamic properties and functions, such as heat capacity and entropy [1]. On the microscopic

L. Vietze · M. Bonn (✉) · M. Grechko
Department of Molecular Spectroscopy, Max Planck Institute for Polymer Research,
Ackermannweg 10, 55128 Mainz, Germany
e-mail: bonn@mpip-mainz.mpg.de

© Springer Nature Singapore Pte Ltd. 2019
M. Cho (ed.), *Coherent Multidimensional Spectroscopy*,
Springer Series in Optical Sciences 226,
https://doi.org/10.1007/978-981-13-9753-0_9

scale, thermal fluctuations actuate the exchange between molecular conformations [2, 3] and can even break covalent bonds [4], promoting chemical reactions. In contrast, vibrational modes with energy quanta (frequency) significantly bigger than kT are usually not thermally excited, and their contribution to molecular thermodynamics is rather small. However, such modes can be populated transiently in a chemical reaction, facilitating energy relaxation and dissipation. In chemistry and biology, such modes are often used, due to their sensitivity, as probes of the molecular environment, conformation, and fluctuations. Thus, based on their energy quanta ω_i , we can classify molecular vibrations into two groups—low-frequency modes (LFMs, with low ω_i) and high-frequency modes (HFMs, with high ω_i).

Around room temperature ($T \approx 25^\circ\text{C}$), which is typical for many chemical and biological systems, the thermal energy $kT \approx 200\text{ cm}^{-1}$. At this temperature the energy of $\sim 1000\text{ cm}^{-1}$ separates the states with a population of >1 and $<1\%$, and we can use this energy as a criterion for our classification of LFMs ($\omega_i < 1000\text{ cm}^{-1}$) and HFMs ($\omega_i > 1000\text{ cm}^{-1}$). With this classification, the frequencies of the LFMs are in the terahertz (far-infrared) frequency range, and those of HFMs are in the mid-infrared frequency range.

In the condensed phase, even as disordered as liquids, HFMs are typically sparse and characteristic for distinct chemical groups. The chemically-specific character of the HFMs stems from their localized nature—usually, these modes are associated with the motion of only a few atoms. For example, the O–H stretch, C–H stretch, C=O stretch vibrations mainly involve two to three atoms. In an absorption spectrum, these modes generate well-resolved peaks and are widely used to characterize the chemical and structural composition of a sample.

In contrast, the LFMs are often very broad and overlap even for chemically simple materials, such as water. These modes are typically collective and delocalized, i.e., they involve the motion of several to many atoms (for example phonons). On the one hand, the collective nature of the LFMs makes them attractive probes of material properties on the microscopic scale. In particular, intermolecular LFMs can provide information on the intermolecular forces and configurations [5]. On the other hand, analysis of the absorption spectra in the terahertz (far-infrared) spectral range is usually extremely challenging because of the spectral congestion, large anharmonicity and thermal population of the LFMs.

From 2D IR spectroscopy, we know that measuring correlations for molecular vibrations can greatly facilitate the analysis [6]. For instance, correlations measured by 2D IR spectroscopy for the same vibrational mode can distinguish homogeneous and inhomogeneous broadening of that vibrational mode. Correlations between different modes measured by cross-peaks in the 2D IR spectrum reflect the coupling between the corresponding motions, which reveals the otherwise hidden dynamics and can greatly assist in elucidating the molecular structure.

Inspired by the advances in the 2D IR spectroscopy, one can expect that resolving the correlations between LFMs can facilitate their analysis as well, and reveal their nature. To this end, measuring correlations between the LFMs and HFMs can be particularly beneficial. Such correlations can provide two types of information. On the one hand, from the HFM perspective, the coupling between the LFMs and HFMs

provides information on important HFM dynamics, including the energy relaxation and dephasing mechanisms and rates. On the other hand, from the LFM perspective, the coupling can provide insight into how LFMs are related to specific chemical groups inside a complex molecular material, thus enabling a “chemically-resolved” spectroscopy of the delocalized, and less chemically specific LFMs.

We note that the coupling between the LFMs and HFMs is indirectly measured by spectral diffusion in the 2D IR spectra. However, to clarify which LFM is affecting the HFM requires modeling and, typically, temperature dependent measurements. The direct measurement of the coupling between the HFMs and LFMs is therefore highly desirable.

To directly measure the coupling between the LFMs and HFMs, we have extended the approach of the 2D DOVE spectroscopy [7–9] by developing two-dimensional Terahertz-InfraRed-Visible (2D TIRV) spectroscopy. This nonlinear spectroscopy technique measures cross-peaks between the LFMs and HFMs (Fig. 9.1) and is based on the resonant enhancement of four-wave mixing of the terahertz (THz), infrared (IR) and visible (VIS) electromagnetic pulses in a sample. In the following sections, we discuss the experimental implementation and theoretical formalism for the 2D TIRV spectroscopy. We illustrate the utilization of the 2D TIRV spectroscopy by the studies of vibrational coupling in liquid water and hybrid organic-inorganic perovskite semiconductors.

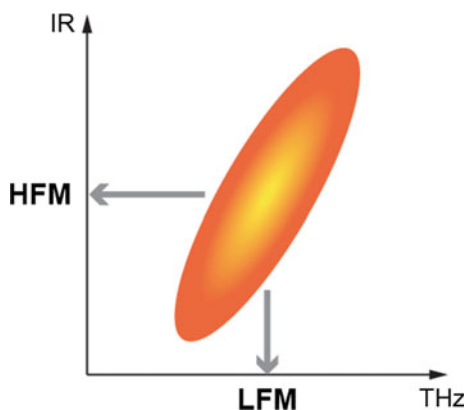


Fig. 9.1 Schematic diagram of a 2D TIRV spectrum. The abscissa axis represents the frequencies of the LFMs in the terahertz frequency range. The ordinate axis is associated with the frequencies of the HFMs in the mid-infrared frequency range. A cross-peak in this 2D plot reflects the coupling between the LFM and HFM. The center line slope of the cross-peak indicates a positive correlation between the frequencies of the HFM and LFM due to the inhomogeneity of the system

9.2 Experimental Implementation

To measure cross-peaks between the LFMs and HFMs, one needs to generate a signal which is enhanced by resonances with both LFM and HFM transitions. The lowest-order optical process that allows generating such signals, and is not forbidden in centrosymmetric materials, is four-wave mixing (FWM), with at least one beam at THz and one at IR frequencies. Although different excitation schemes can be employed for 2D TIRV spectroscopy, we use the excitation scheme shown in Fig. 9.2a. In this scheme, the interaction of a material with the THz, IR and VIS pulses (Fig. 9.2b)—each interacting once with the sample—generates a nonlinear polarization which emits the signal. The polarization and, thus, the signal, is enhanced by the resonances with the LFMs ($|1\rangle$) and HFMs ($|2\rangle$), given that there is coupling between these vibrational modes. The advantage of this excitation scheme is that it uses only one interaction between the sample and the usually weak THz pulse. This results in a more intense signal compared to the schemes which employ two interactions between the sample and the THz electromagnetic field. Also, using the VIS pulse produces a signal at visible frequencies (600–700 nm), where very sensitive detectors are available.

Our experimental 2D TIRV setup is shown schematically in Fig. 9.3. The output of an amplified femtosecond Ti:Sapphire laser with 1 kHz repetition rate and a central wavelength of 800 nm (60 nm full width at half maximum, FWHM) is split into *beam 1* (≈ 1 mJ/pulse), *2* (≈ 0.4 mJ/pulse) and *3* (≈ 1 mJ/pulse) to generate the IR, VIS and THz pulses, respectively.

Beam 1 pumps a TOPAS (traveling-wave optical parametric amplifier) system, which generates a broadband IR beam (~ 400 cm^{-1} FWHM) with a tunable center frequency. The center frequency of the IR is tuned in resonance with the HFMs of the sample. To produce the VIS beam, we spectrally narrow *beam 2* to ~ 30 cm^{-1} FWHM by passing it through a Fabry-Pérot interferometer (FPI). We combine the IR and the VIS beams using a beam combiner (BC) and focus them using a 20 cm CaF_2 lens (LI). For our measurements, we use an optical configuration in which the focus of the IR beam is at the sample, and the VIS beam is focused 1.5 cm in front of the sample. We use *beam 3* to generate the broadband THz pulse by two-color

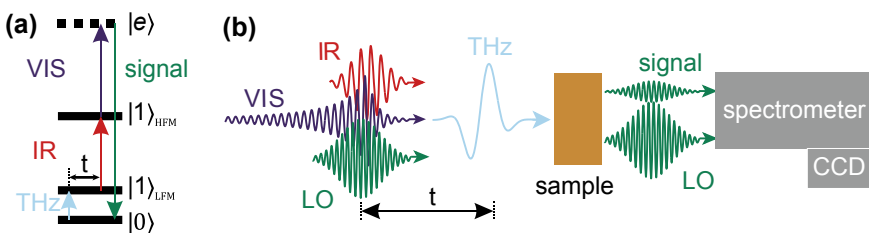


Fig. 9.2 **a** Energy level diagram for the four-wave mixing light-matter interactions used in 2D TIRV spectroscopy. **b** Scheme of 2D TIRV spectroscopy demonstrating the electromagnetic pulses used in the four-wave mixing and detection of the signal

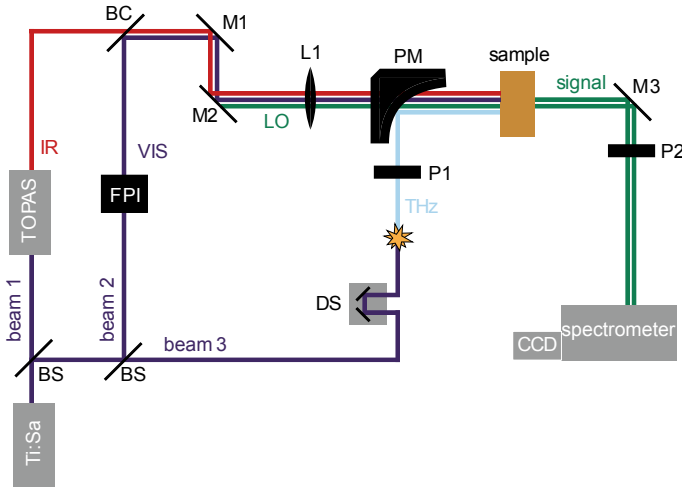


Fig. 9.3 Layout of the setup for 2D TIRV spectroscopy. The setup consists of the following optical and optomechanical components: beam combiner (*BC*); beam splitter (*BS*), protected gold-coated mirrors (*M1*, *M2*, and *M3*); lens (1); parabolic mirror (*PM*); delay stage (*DS*); THz polarizer (*P1*); optical polarizer (*P2*); Fabry-Pérot interferometer (*FPI*); spectrometer and detector (*CCD* camera)

femtosecond laser mixing in gas plasma [10–12]. To this end, we focus *beam 3* in air using a lens ($f = 20$ cm). The focused femtosecond pulse produces air plasma. About 5 cm before the focus we install a $100\ \mu\text{m}$ thick beta barium borate (β -BBO) crystal on the beam pathway to generate the second harmonic of the *pulse 3*. Mixing of the ultrafast 800 nm and 400 nm electromagnetic fields in the air plasma results in the emission of a coherent and spectrally broad THz pulse ($20\text{--}450\ \text{cm}^{-1}/0.6\text{--}13\ \text{THz}$). The THz pulse is focused at the sample by the parabolic mirror (*PM*), and spatially overlapped with the IR and VIS beams. An optical delay stage (*DS*) allows to control the temporal delay between the terahertz pulse and the IR/VIS pulse pair.

Four-wave mixing (FWM) of the THz, IR and VIS electromagnetic fields in the sample generates a signal at visible frequencies ($\omega_{\text{VIS}} + \omega_{\text{IR}} \pm \omega_{\text{THz}}$). For 2D TIRV spectroscopy we measure the electric field of the signal, rather than its intensity. To this end, we use heterodyne detection by mixing the signal field with the local oscillator (*LO*) field. The latter is produced by sum-frequency generation of the IR and VIS pulses at the mirrors *M1* and *M2* (Fig. 9.3). The signal and the LO are aligned to the spectrometer, and a spectrally resolved interference of these two fields is measured by a CCD camera.

A 2D TIRV spectrum has the frequency axes ω_1 and ω_2 . As explained in detail in the next section, the ω_2 frequencies are associated with the HFM resonances and the ω_1 frequencies reflect the LFM resonances in the sample. To derive the ω_2 axis we subtract the frequency of the VIS pulse from the frequency of the signal, which is given by the spectrometer. The ω_1 axis is obtained by the time-domain approach. For this, we measure the signal field (interference between the signal and LO) for different time delays t between the THz pulse and the IR/VIS pulse pair.

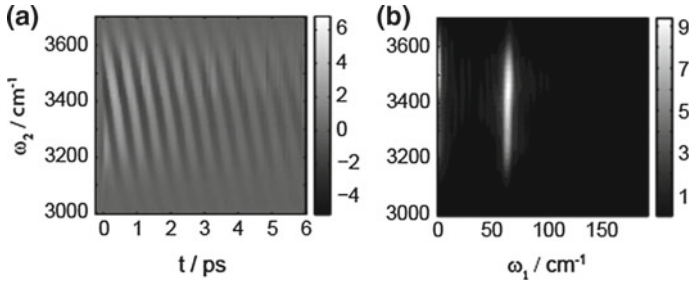


Fig. 9.4 2D TIRV data for the model sample—a CaF_2 crystal. **a** The time-domain 2D TIRV data is given by the interference between the signal and the local oscillator at different time delays t . **b** The absolute-value 2D TIRV spectrum is obtained by a Fourier transform of the time-domain data of **(a)**

The working principle underlying 2D TIRV spectroscopy can be nicely demonstrated by a CaF_2 model sample. In the CaF_2 crystal, the short THz pulse coherently excites phonon modes. The evolution of the excited phonon polarization is probed at varying time delays t by the IR/VIS pulse pair, as shown in Fig. 9.4a. The 2D TIRV spectrum can be derived from the time-domain data by Fourier transforming along the time axis t (for each ω_2 frequency), to obtain the ω_1 frequencies.

As shown in Fig. 9.4b, the absolute-value 2D TIRV spectrum of CaF_2 has one peak. Location and linewidth of this peak along the ω_1 axis are determined by, respectively, the frequency (67 cm^{-1}) and lifetime ($\sim 3 \text{ ps}$) of the excited phonon coherence. Because the interaction with the IR field is non-resonant for CaF_2 , the location and linewidth of the peak along the ω_2 axis are determined by the central frequency and bandwidth of the IR pulse, respectively.

9.3 Theoretical Formalism

In optical spectroscopies, molecular properties determine the linear and non-linear response functions $S^{(1)}$ and $S^{(n)}$, respectively. Deducing molecular properties from the experimental spectra requires, first of all, knowledge of the relationship between the signal measured by the detector and the corresponding response function of a sample. The same is true also for 2D TIRV spectroscopy, for which we need to determine how the signal at the detector relates to the third-order non-linear response function $S^{(3)}$ of the material. In the present section, we derive this relationship and illustrate it with a few theoretical model examples.

The electric field $E^{(3)}$ of the 2D TIRV signal is emitted by a sample after three interactions with the three relevant electromagnetic fields: one with the THz, one with the IR and one with the VIS pulse. The signal field is proportional to the third-order non-linear polarization generated by the material-light interactions. Thus, by employing the frequency domain formalism for the third-order nonlinear response

function ((5.32) in [13]) we obtain the signal field for a time delay τ of the THz pulse:

$$E^{(3)}(t, \tau) \propto \iiint d\omega_1 d\omega_2 d\omega_3 S^{(3)}(\omega_1 + \omega_2 + \omega_3, \omega_1 + \omega_2, \omega_1) E_{\text{THz}}(\omega_1) e^{-i\omega_1 \tau} E_{\text{IR}}(\omega_2) E_{\text{VIS}}(\omega_3) e^{-i\omega_s t}, \quad (9.1)$$

where t is the time; frequency $\omega_s = \omega_1 + \omega_2 + \omega_3$; $E_{\text{THz}}(\omega_1)$, $E_{\text{IR}}(\omega_2)$ and $E_{\text{VIS}}(\omega_3)$ are electric fields of the THz, IR and VIS pulses at the frequencies ω_1 , ω_2 and ω_3 , respectively. We note that the integration in (9.1) is performed from $-\infty$ to $+\infty$, i.e. the frequencies take on both negative and positive values. In (9.1) the field $E^{(3)}$ changes with the time t and depends parametrically on the time delay τ : the time-dependent field is calculated for each delay time τ . In our experiment we use a local oscillator (LO) for the heterodyne detection of the signal. Thus, the total electromagnetic wave after the sample is:

$$E^{\text{tot}}(t, \tau) = E_{\text{LO}}(t) + E^{(3)}(t, \tau) \propto E_{\text{LO}}(t) + \iiint d\omega_1 d\omega_2 d\omega_3 S^{(3)}(\omega_1 + \omega_2 + \omega_3, \omega_1 + \omega_2, \omega_1) E_{\text{THz}}(\omega_1) e^{-i\omega_1 \tau} E_{\text{IR}}(\omega_2) E_{\text{VIS}}(\omega_3) e^{-i\omega_s t}, \quad (9.2)$$

where $E_{\text{LO}}(t)$ is the electric field of the local oscillator. These combined fields are guided to the spectrometer, where they are dispersed by the grating. This dispersion is mathematically described by a Fourier transform of the field $E^{\text{tot}}(t, \tau)$ over time t :

$$\begin{aligned} E^{\text{tot}}(\Omega'_3, \tau) &= \text{FT}[E_{\text{LO}}(t) + E^{(3)}(t, \tau)] \propto E_{\text{LO}}(\Omega'_3) + E^{(3)}(\Omega'_3, \tau) \\ &= E_{\text{LO}}(\Omega'_3) \\ &\quad + \iiint d\omega_1 d\omega_2 d\omega_3 S^{(3)}(\omega_1 + \omega_2 + \omega_3, \omega_1 + \omega_2, \omega_1) \\ &\quad E_{\text{THz}}(\omega_1) e^{-i\omega_1 \tau} E_{\text{IR}}(\omega_2) E_{\text{VIS}}(\omega_3) \delta(\Omega'_3 - \omega_s), \end{aligned} \quad (9.3)$$

where $E_{\text{LO}}(\Omega'_3)$ is the electric field of the LO at frequency Ω'_3 and δ is the Dirac delta function. The frequency Ω'_3 in (9.3) can have both positive and negative values. After the grating, spectral components of light at $+\Omega'_3$ and $-\Omega'_3$ travel in the same direction. This co-propagation of spectral components at frequencies with opposite sign ensures that the electromagnetic field is a real-valued function of space and time coordinates. The signal intensity A measured by the square-law detector (CCD camera) for the detection frequency $\Omega_3 \geq 0$ and integrated over accumulation time period T is given by:

$$A(\Omega_3, \tau) \propto \int_T dt [E^{\text{tot}}(\Omega_3, \tau) e^{-i\Omega_3 t} + E^{\text{tot}}(-\Omega_3, \tau) e^{i\Omega_3 t}]^2$$

$$\begin{aligned}
&= \int_T dt \left[E^{(3)}(\Omega_3, \tau) e^{-i\Omega_3 t} + E^{(3)}(-\Omega_3, \tau) e^{i\Omega_3 t} \right. \\
&\quad \left. + E_{\text{LO}}(\Omega_3) e^{-i\Omega_3 t} + E_{\text{LO}}(-\Omega_3) e^{i\Omega_3 t} \right]^2. \quad (9.4)
\end{aligned}$$

By squaring the term under the integral, neglecting terms oscillating at very high frequency ($\sim 2\Omega_3$) and subtracting the homodyne terms of the form $E^{(3)}(\Omega_3, \tau)E^{(3)}(-\Omega_3, \tau)$ and $E_{\text{LO}}(\Omega_3)E_{\text{LO}}(-\Omega_3)$ we obtain the heterodyne-detected part B of the measured signal (B represents the interference between the signal field and the LO):

$$B(\Omega_3, \tau) \propto E^{(3)}(\Omega_3, \tau)E_{\text{LO}}(-\Omega_3) + E^{(3)}(-\Omega_3, \tau)E_{\text{LO}}(\Omega_3). \quad (9.5)$$

The heterodyne-detected signal depends parametrically on the time delay τ of the THz pulse. In the experiment, this dependence appears in the time-domain 2D TIRV data. In order to obtain the 2D TIRV spectrum $\Gamma(\Omega_3, \Omega_1)$ as a function of the detection frequency Ω_3 and the THz frequency Ω_1 we Fourier transform $B(\Omega_3, \tau)$ over τ :

$$\begin{aligned}
\Gamma(\Omega_3, \Omega_1) &= \text{FT}[B(\Omega_3, \tau)] \\
&\propto \text{FT}[E^{(3)}(\Omega_3, \tau)]E_{\text{LO}}(-\Omega_3) + \text{FT}[E^{(3)}(-\Omega_3, \tau)]E_{\text{LO}}(\Omega_3) \\
&= E^{(3)}(\Omega_3, \Omega_1)E_{\text{LO}}(-\Omega_3) + E^{(3)}(-\Omega_3, \Omega_1)E_{\text{LO}}(\Omega_3). \quad (9.6)
\end{aligned}$$

Using (9.3) we obtain for $E^{(3)}(\Omega_3, \Omega_1)$:

$$\begin{aligned}
E^{(3)}(\Omega_3, \Omega_1) &= \text{FT}[E^{(3)}(\Omega_3, \tau)] \\
&\propto \iiint d\omega_1 d\omega_2 d\omega_3 S^{(3)}(\omega_1 + \omega_2 + \omega_3, \omega_1 + \omega_2, \omega_1) \\
&\quad E_{\text{THz}}(\omega_1)\delta(\Omega_1 - \omega_1)E_{\text{IR}}(\omega_2)E_{\text{VIS}}(\omega_3)\delta(\Omega_3 - \omega_s). \quad (9.7)
\end{aligned}$$

In the experiment, we use a narrowband VIS pulse with the frequency Ω_{VIS} . Note that Ω_{VIS} is a parameter rather than a variable, and we assume $\Omega_{\text{VIS}} > 0$. Thus, we approximate the VIS spectrum by a delta function:

$$E_{\text{VIS}}(\omega_3) = \delta(\Omega_{\text{VIS}} - \omega_3) + \delta(\Omega_{\text{VIS}} + \omega_3). \quad (9.8)$$

By substituting (9.8) into (9.7) and performing the integration, we obtain:

$$\begin{aligned}
E^{(3)}(\Omega_3, \Omega_1) &\propto S^{(3)}(\Omega_3, \Omega_3 - \Omega_{\text{VIS}}, \Omega_1)E_{\text{THz}}(\Omega_1)E_{\text{IR}}(\Omega_3 - \Omega_{\text{VIS}} - \Omega_1) \\
&\quad + S^{(3)}(\Omega_3, \Omega_3 + \Omega_{\text{VIS}}, \Omega_1)E_{\text{THz}}(\Omega_1)E_{\text{IR}}(\Omega_3 + \Omega_{\text{VIS}} - \Omega_1). \quad (9.9)
\end{aligned}$$

Because in our experiment the THz frequency $\Omega_1 \ll \Omega_3 + \Omega_{\text{VIS}}$, the frequency $\Omega_3 + \Omega_{\text{VIS}} - \Omega_1$ is beyond the bandwidth of the IR pulse. Thus, $E_{\text{IR}}(\Omega_3 + \Omega_{\text{VIS}} - \Omega_1) = 0$ and the second term in (9.9) vanishes. Similarly, for

$E^{(3)}(-\Omega_3, \Omega_1)$ we obtain:

$$E^{(3)}(-\Omega_3, \Omega_1) \propto S^{(3)}(-\Omega_3, -\Omega_3 + \Omega_{\text{VIS}}, \Omega_1) E_{\text{THz}}(\Omega_1) E_{\text{IR}}(-\Omega_3 + \Omega_{\text{VIS}} - \Omega_1). \quad (9.10)$$

By substituting (9.10) and (9.9) into (9.6) we obtain for the 2D TIRV spectrum:

$$\begin{aligned} \Gamma(\Omega_3, \Omega_1) \propto & S^{(3)}(\Omega_3, \Omega_3 - \Omega_{\text{VIS}}, \Omega_1) E_{\text{THz}}(\Omega_1) E_{\text{IR}}(\Omega_3 - \Omega_{\text{VIS}} - \Omega_1) E_{\text{LO}}(-\Omega_3) \\ & + S^{(3)}(-\Omega_3, -\Omega_3 + \Omega_{\text{VIS}}, \Omega_1) E_{\text{THz}}(\Omega_1) E_{\text{IR}}(-\Omega_3 + \Omega_{\text{VIS}} - \Omega_1) E_{\text{LO}}(\Omega_3). \end{aligned} \quad (9.11)$$

For the sake of convenience, we introduce the frequency $\Omega_2 = \Omega_3 - \Omega_{\text{VIS}}$, which is in the IR frequency range, to write (9.11) in the alternative form:

$$\begin{aligned} \Gamma(\Omega_2 + \Omega_{\text{VIS}}, \Omega_1) \propto & S^{(3)}(\Omega_2 + \Omega_{\text{VIS}}, \Omega_2, \Omega_1) E_{\text{THz}}(\Omega_1) E_{\text{IR}}(\Omega_2 - \Omega_1) E_{\text{LO}}(-\Omega_2 - \Omega_{\text{VIS}}) \\ & + S^{(3)}(-\Omega_2 - \Omega_{\text{VIS}}, -\Omega_2, \Omega_1) E_{\text{THz}}(\Omega_1) E_{\text{IR}}(-\Omega_2 - \Omega_1) E_{\text{LO}}(\Omega_2 + \Omega_{\text{VIS}}). \end{aligned} \quad (9.12)$$

Thus, in the experiment, the 2D TIRV spectrum is given by the product of the spectrum of the third-order nonlinear response function $S^{(3)}$ with the spectra E_{THz} and E_{IR} of the laser pulses. From (9.12) it follows that Ω_1 and Ω_2 are the frequencies of the coherences excited in the sample after interaction with the THz and the IR pulses, respectively. Because the VIS pulse is narrowband with frequency Ω_{VIS} , it is convenient and more informative to plot the 2D TIRV spectrum $\Gamma(\Omega_3, \Omega_1)$ as a function of the Ω_1 and Ω_2 frequencies, i.e., $\Gamma(\Omega_2, \Omega_1)$ by subtracting Ω_{VIS} from the detection frequency Ω_3 . The advantage of doing so is that the Ω_2 frequencies reflect the HFMs resonances of the sample.

Equation 9.12 shows that the 2D TIRV spectra in our experiment are produced by the sum of the $S^{(3)}$ spectra in the two quadrants, (Ω_2, Ω_1) and $(-\Omega_2, \Omega_1)$. This is due to the utilization of the spectrometer to measure the second frequency axis and is analogous to the summation of the rephasing and non-rephasing spectra in the 2D IR spectroscopy employing the pump-probe geometry and a spectrometer.

Let us next consider the spectrum of the response function $S^{(3)}$ for a simple model of two coupled modes, one LFM and one HFM (Fig. 9.5). Figure 9.6 shows four different Liouville excitation pathways for this model. In diagrams **I** and **II**, the interactions with the THz, IR and VIS fields are all on the ket side of the density matrix. Thus, these diagrams represent the sum-frequency generation between all the three beams (first and second terms in (9.12) for $\Omega_1 > 0$ and $\Omega_1 < 0$, respectively). The first two diagrams are distinct in the following manner:

- In diagram **I**, the interactions with the THz and IR fields excite the LFM and HFM, respectively. These excitations are one-quantum transitions, i.e. they change only one vibrational quantum number of the sample at a time. In contrast, at either transition to the excited electronic state $|e\rangle$ induced by the VIS pulse or at the signal

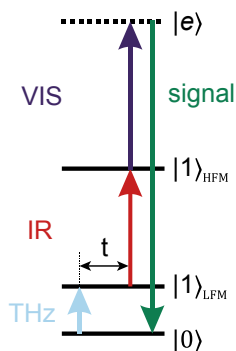


Fig. 9.5 Energy level diagram for the two interacting low-frequency ($|1\rangle_{LFM}$) and high-frequency ($|1\rangle_{HFM}$) vibrational states. Generally speaking, the transition to the electronically excited state $|e\rangle$ can be resonant or non-resonant. In the latter case, the state $|e\rangle$ is usually called a virtual state

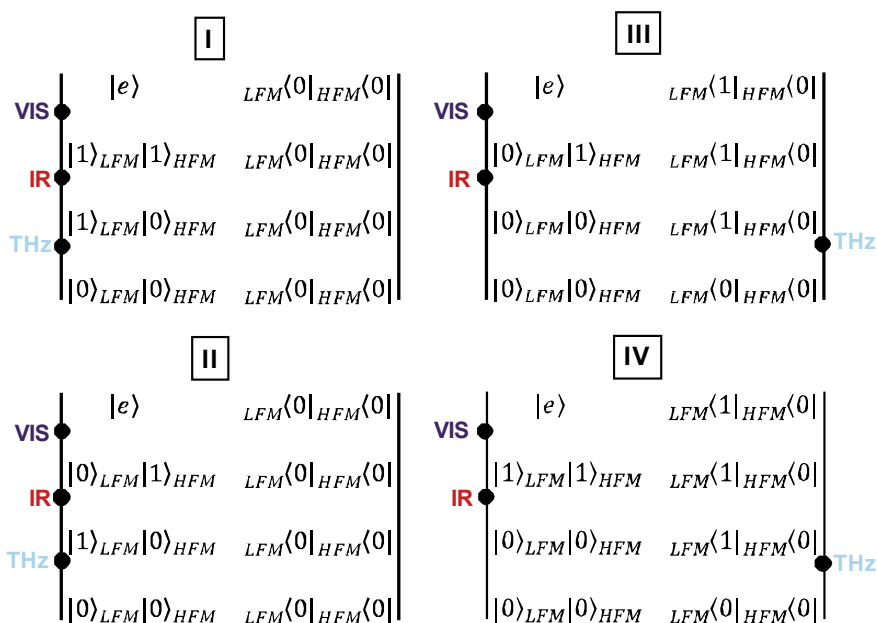


Fig. 9.6 Liouville excitation pathways for the 2D TIRV spectroscopy of the model in Fig. 9.5. Interactions with the laser fields are indicated by *black circles*. The diagrams **I** and **II** (**III** and **IV**) correspond to the $\omega_{VIS} + \omega_{IR} + \omega_{THz}$ ($\omega_{VIS} + \omega_{IR} - \omega_{THz}$) four-wave mixing

emission the sample undergoes a two-quantum transition [7]. This two-quantum transition changes both LFM and HFM quantum numbers simultaneously.

- In diagram **II**, the interaction with the THz pulse excites the LFM mode. The two-quantum transition takes place at the interaction with the IR pulse, which excites the HFM and simultaneously quenches the LFM. The subsequent interaction with the VIS pulse and the signal emission are both one-quantum transitions.

In diagrams **III** and **IV**, the interaction with the THz field occurs on the bra side of the density matrix, and the interactions with the IR and VIS fields are on the ket side. Thus, these diagrams represent signal generation at the sum frequency of the IR and VIS pulses minus frequency of the THz pulse.

- Similar to diagram **I**, in diagram **III**, the interactions with the THz and IR fields excite the LFM and HFM, and the two-quantum transition occurs at the interaction with the VIS pulse as well as for the emission of the signal field.
- Similar to diagram **II**, in diagram **IV**, the THz pulse excites the LFM and the IR pulse induces the two-quantum transition—it simultaneously excites the HFM and the LFM on the ket side of the density matrix. Both the interaction with the VIS pulse and the signal emission proceed via one-quantum transitions.

For all four diagrams in Fig. 9.6 there are complex-conjugate pathways, which can be obtained by changing all interactions from the ket to the bra side of the density matrix and vice versa. Because at least one of the transitions involves a simultaneous change of the vibrational quantum numbers for the HFM and LFM, the 2D TIRV signal requires a coupling between these modes [7, 8]. The coupling can originate from either the mechanical and/or electrical anharmonicity between the vibrations [14].

In our model, we assume the fast modulation (homogeneous) limit for the frequency fluctuation correlation function [6]. The temporal evolution of the LFM coherence $|\rho(t) \gg_{\text{LFM}}$ with the initial conditions $|\rho(0) \gg_{\text{LFM}} = |1\rangle_{\text{LFM}}|0\rangle_{\text{HFM}}|0\rangle_{\text{HFM}}$ is given by:

$$|\rho(t) \gg_{\text{LFM}} = \exp\left(-i\frac{E_{\text{LFM}}}{\hbar}t - \frac{1}{T_{\text{LFM}}}t\right)|\rho(0) \gg_{\text{LFM}},$$

where T_{LFM} is the LFM coherence lifetime and E_{LFM} is the energy of the LFM. Similarly, for the HFM coherence with the initial conditions $|\rho(0) \gg_{\text{HFM}} = |0\rangle_{\text{LFM}}|1\rangle_{\text{HFM}}|0\rangle_{\text{HFM}}$:

$$|\rho(t) \gg_{\text{HFM}} = \exp\left(-i\frac{E_{\text{HFM}}}{\hbar}t - \frac{1}{T_{\text{HFM}}}t\right)|\rho(0) \gg_{\text{HFM}},$$

where T_{HFM} is the HFM coherence lifetime and E_{HFM} is the energy of the HFM. For the coherence $|\rho(t) \gg_e$ in the electronically excited state $|e\rangle$ we assume that the time dependence can be described by:

$$|\rho(t)\rangle\rangle_e = \exp\left(-i\frac{E_e}{\hbar}t - \frac{1}{T_e}t\right)|\rho(0)\rangle\rangle_e,$$

where T_e is the electronic coherence lifetime, E_e is the energy of the excited electronic state $|e\rangle$ and $|\rho(0)\rangle\rangle_e$ is the initial condition for the electronic coherence.

We assume that the two-quantum transition occurs at the interaction with the IR pulse. Thus the Liouville excitation pathways are given by the diagrams **II** and **IV** in Fig. 9.6. Using the equations above, we can write for the response function in diagram **II**:

$$S_{\text{II}}^{(3)}(t_3, t_2, t_1) = \left(\frac{i}{\hbar}\right)^3 \mu_1 \mu_2 \mu_3 \mu_4 \exp\left(-i\frac{E_e}{\hbar}t_3 - \frac{1}{T_e}t_3\right) \exp\left(-i\frac{E_{\text{HFM}}}{\hbar}t_2 - \frac{1}{T_{\text{HFM}}}t_2\right) \exp\left(-i\frac{E_{\text{LFM}}}{\hbar}t_1 - \frac{1}{T_{\text{LFM}}}t_1\right) \quad (13)$$

where μ_1, μ_2, μ_3 and μ_4 are the transition dipole moments for the THz, IR, VIS excitations and the signal emission, respectively. Figure 9.7 shows the spectrum $S_{\text{II}}^{(3)}(\Omega_2, \Omega_1)$. For this simulation, we have assumed non-resonant conditions for the electronic transition ($\frac{E_e}{\hbar} - \frac{1}{T_e} \gg \Omega_3 = \Omega_2 + \Omega_{\text{VIS}}$) and use the following parameters: $\frac{E_{\text{LFM}}}{\hbar} = 50 \text{ cm}^{-1}$, $T_{\text{LFM}} = 300 \text{ fs}$, $\frac{E_{\text{HFM}}}{\hbar} = 3000 \text{ cm}^{-1}$, $T_{\text{HFM}} = 150 \text{ fs}$. The spectrum $S_{\text{II}}^{(3)}(\Omega_2, \Omega_1)$ has a maximum in the first quadrant, i.e., when $\Omega_1 > 0$ and $\Omega_2 > 0$. Similarly, we can calculate the spectrum $S_{\text{IV}}^{(3)}(\Omega_2, \Omega_1)$, which has a maximum in the second quadrant, i.e., for $\Omega_1 < 0$ and $\Omega_2 > 0$. The third and the fourth quadrants are dominated by the complex conjugate responses $(S_{\text{II}}^{(3)}(\Omega_2, \Omega_1))^*$ and $(S_{\text{IV}}^{(3)}(\Omega_2, \Omega_1))^*$, respectively.

By taking into account $S_{\text{II}}^{(3)}(\Omega_2, \Omega_1)$, $S_{\text{IV}}^{(3)}(\Omega_2, \Omega_1)$, $(S_{\text{II}}^{(3)}(\Omega_2, \Omega_1))^*$, $(S_{\text{IV}}^{(3)}(\Omega_2, \Omega_1))^*$ and assuming infinitely broad spectra for the THz, IR and

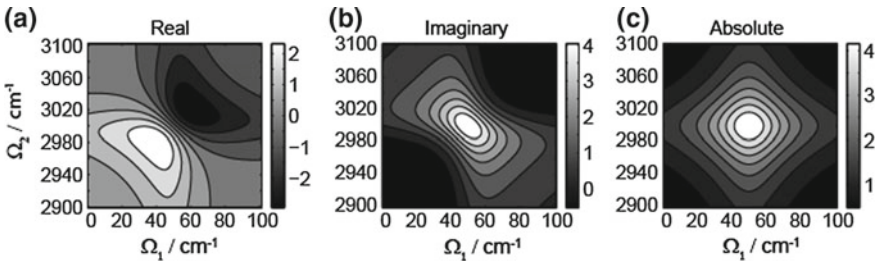


Fig. 9.7 Real- (a), imaginary- (b), and absolute-value (c) spectra for the third order non-linear response function $S_{\text{II}}^{(3)}(\Omega_2, \Omega_1)$ for the model of two coupled LFM and HFM oscillators. The LFM oscillator has a frequency of 50 cm^{-1} and decay time of 300 fs. The HFM oscillator has a frequency of 3000 cm^{-1} and a decay time of 150 fs

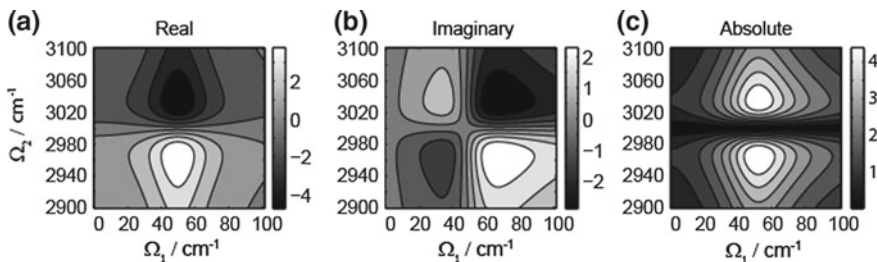


Fig. 9.8 Real- (a), imaginary (b) and absolute-value (c) spectra $\Gamma(\Omega_2, \Omega_1)$ for the model of two coupled LFM and HFM oscillators. The LFM and HFM oscillators have frequencies (lifetimes) of 50 cm^{-1} (300 fs) and 3000 cm^{-1} (150 fs), respectively

LO pulses, we can calculate $\Gamma(\Omega_2, \Omega_1)$ using (9.11) (Fig. 9.8). Note that in the spectrum $\Gamma(\Omega_2, \Omega_1)$ the responses in the first ($S_{\text{II}}^{(3)}(\Omega_2, \Omega_1)$) and fourth ($S_{\text{IV}}^{(3)}(\Omega_2, \Omega_1)$)* quadrants add up destructively the central frequency of the HFM and produce a nodal line.

9.4 Application: Vibrational Coupling in Water

In liquid water, hydrogen bonding between the molecules arranges them into a short-lived (about 1 ps lifetime) local tetrahedral structure where each molecule donates and accepts, on average, about 3.6 hydrogen bonds [15, 16]. The intermolecular distances and relative orientations of the molecules in the local structure fluctuate on sub-picosecond time-scales [17–19]. These fluctuations constitute the low-frequency intermolecular vibrational modes of neat water. The fluctuations of the hydrogen bond network affect the high-frequency intramolecular vibrations of the water molecules. The intramolecular O–H stretch vibration is particularly sensitive to the configuration of the hydrogen bond network. The frequency and transition dipole moment of this HFM have, respectively, inverse and direct relationship with the strength of the electric field along the O–H bond, which is created by neighboring molecules [20, 21]. Thus, fluctuations of the hydrogen bond network caused by the LFM perturb the O–H stretch vibration and give rise to the coupling between the LFM and HFMs in liquid water. Recently, a growing number of studies point to a strong mixing between the LFM and O–H stretch modes, implying an active role of such mixed states in the chemistry of water [22–24].

We use 2D TIRV spectroscopy to directly measure the coupling between the water LFM and the O–H stretch vibration [25]. In this study, we focus on the 20–450 cm^{-1} spectral range for the intermolecular vibrations, which comprises mainly the hydrogen bond stretch ($\approx 180 \text{ cm}^{-1}$) and bending ($\approx 60 \text{ cm}^{-1}$) modes. Figure 9.9 shows the absolute-value 2D TIRV spectra for different isotope dilutions of H_2O in D_2O . The spectra for the 5% and 20% H/D ratio are similar and have one dominating

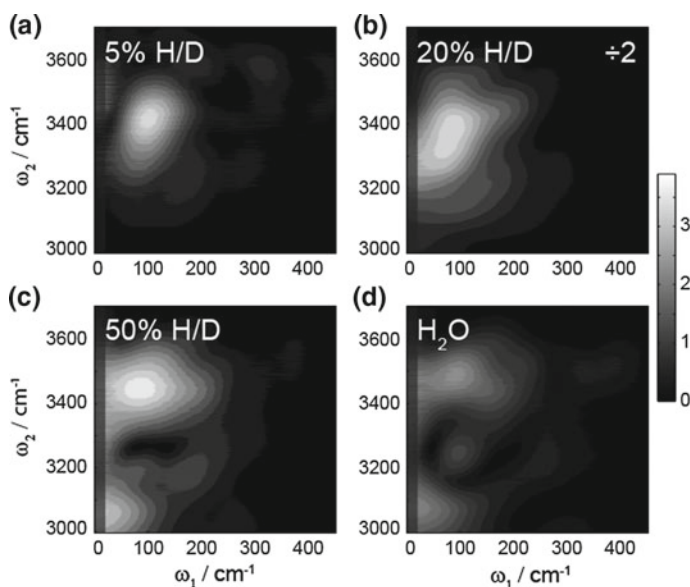


Fig. 9.9 Absolute-value 2D TIRV spectra for **a** 5% H/D, **b** 20% H/D, **c** 50% H/D and **d** 100% H₂O samples

peak. This peak is centered at $\omega_1 \approx 100 \text{ cm}^{-1}$, $\omega_2 \approx 3415 \text{ cm}^{-1}$ for the 5% sample and shifts to the slightly lower ω_2 ($\omega_2 \approx 3370 \text{ cm}^{-1}$) with an increase of the proton concentration to 20%. But when the proton concentration increases further, to 50 and 100%, the line shape of the 2D TIRV spectrum changes substantially. This change is characterized by a significant broadening of the response to the lower ω_2 frequencies and the appearance of a nodal line at $\omega_2 \approx 3270 \text{ cm}^{-1}$. Because the spectrum of the water LFMs in the 20–450 cm^{-1} frequency range changes only slightly with the change of the H/D ratio, the variation of the 2D TIRV spectrum is due to the new character of the O–H stretch vibration. This variation is caused by two different phenomena: (1) Fermi resonance between the O–H stretch and H–O–H bending modes; (2) excitonic intermolecular delocalization of the O–H stretch vibration. The excitonic delocalization stems from the increasing coupling between the O–H stretch oscillators with increasing proton concentration because of the higher concentration of the OH groups and the resulting smaller average distance between OH groups. The 5% H/D sample contains ~90% of D₂O molecules, 9.5% of HOD and 0.0025% of H₂O molecules. For this sample, the majority of the OH groups are separated and decoupled by D₂O molecules. Thus, the 2D TIRV spectrum for the 5% H/D sample reflects a vibrational coupling for the isolated O–H stretch oscillator. With increasing proton concentration, the average distance between the oscillators decreases—note that neighboring OH groups can be located in the same molecule (H₂O) or in the adjacent HOD/H₂O molecules. The shorter distances result in an increased coupling between the oscillators and an increased average intra- and intermolecular delocalization of the vibration. In addition to the coupling between the

O–H stretch oscillators, H₂O molecules have a Fermi resonance between the O–H stretch and the second excited H–O–H bending state. Increasing concentration of the H₂O species enhances the signal from the mixed stretch-bending states. As a result, the change of the 2D TIRV response can be linked to the appearance of the Fermi resonance and the formation of the vibrational exciton.

A comparison of the experimental 2D TIRV spectra and classical molecular dynamics simulations shows that the broadening of the spectrum to the lower ω_2 frequencies in H₂O is due to the stronger coupling between the LFMs and the red-shifted O–H stretch modes at $\sim 3250\text{ cm}^{-1}$. At the same time, the spectrum of the LFMs coupled with the O–H stretch oscillator is insensitive to the vibrational delocalization and Fermi resonance of the latter. Both isolated and delocalized O–H stretch are predominantly coupled with the broad spectrum of LFMs in the $50\text{--}250\text{ cm}^{-1}$ frequency range, which can be assigned to the hydrogen bond bending ($\approx 60\text{ cm}^{-1}$) and stretching ($\approx 180\text{ cm}^{-1}$) modes.

9.5 Application: Vibrational Coupling in Hybrid Perovskite

The outstanding photovoltaic performance of the perovskite semiconductors has attracted substantial attention, not only for improved devices, but also for the understanding of the fundamental physical properties of these promising materials. In particular, it is intriguing how different degrees of freedom, electronic and nuclear, interplay and influence diverse photophysical properties, such as charge transport, recombination, and hot-carrier relaxation [26]. In this regard, the loosely bound organic molecules inside the inorganic cage of hybrid perovskite are believed to play a substantial role. Although the main discussion in the literature has focused on the direct interaction of the molecular dipole moment with the charge carriers, the vibrational coupling between the organic and inorganic sub-lattices is expected to have an indirect influence on the electronic properties of perovskites.

The low-frequency vibrations in perovskites are the phonon modes of this crystalline material. Previous studies have identified a plethora of the perovskite phonon modes, with energies in the range of $0\text{--}150\text{ cm}^{-1}$ [27, 28]. In fact, the $0\text{--}60\text{ cm}^{-1}$ frequency range in the infrared absorption and Raman spectra of these materials is dominated by the phonons of the inorganic sub-lattice. Vibrations of the perovskite organic sub-lattice are those of the organic ions embedded into the inorganic cage. Some of these molecular motions are collective LFMs with relatively low frequencies, $\sim 60\text{--}150\text{ cm}^{-1}$. Alongside the collective LFMs, the organic ions have localized HFMs, which are specific to the chemical groups composing the ion. For example, methylammonium and formamidinium ions have N–H stretch modes with energies of $\sim 3100\text{--}3450\text{ cm}^{-1}$. A coupling between organic HFMs and inorganic phonons can generate mixed states with relatively high energy and low quantum numbers. Such mixed states can provide additional pathways for the electronic energy relaxation, via strong coupling between the phonon moiety and the excited electronic states [29].

2D TIRV spectroscopy enables a direct measurement of the coupling between the organic HFMs and inorganic LFMs in hybrid perovskites [30]. Figure 9.10 shows experimental spectra for the two prototypical samples, methylammonium lead triiodide (MAPbI₃) and mixed formamidinium methylammonium lead triiodide (FA_{0.8}MA_{0.2}PbI₃). The spectrum of MAPbI₃ has a single peak centered at $\omega_1 = 35 \text{ cm}^{-1}$, $\omega_2 = 3135 \text{ cm}^{-1}$, which reflects the coupling between the symmetric and asymmetric N–H stretch vibrations of the MA⁺ on the one hand and the phonon mode on the other. Replacing MA⁺ by the FA⁺ results in a change of the 2D TIRV line shape along both the ω_1 and ω_2 axes. The change of the spectral profile along the ω_2 axis is in accordance with the difference of the N–H stretch absorption spectra for FA⁺ and MA⁺. However, the spectral change along the ω_1 axis is in sharp contrast to the almost identical phonon modes in the two types of perovskite. This indicates that the coupling between the N–H stretch mode and the phonons depend not only on the existing phonon vibrations, but also on the structure of the organic cation.

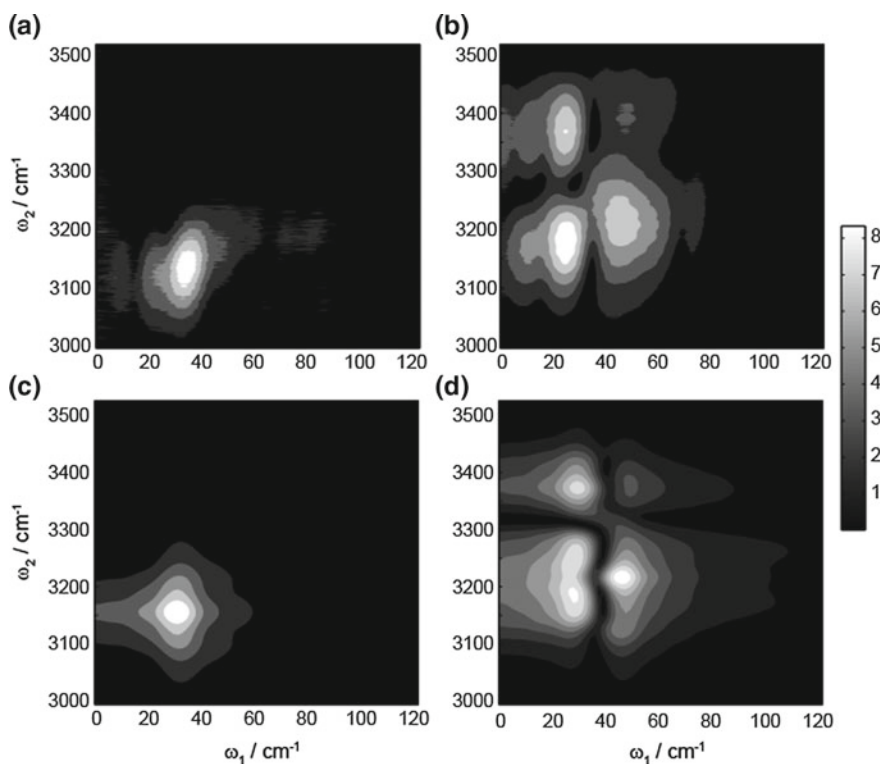


Fig. 9.10 Absolute-value measured 2D TIRV spectra for **a** MAPbI₃ and **b** FA_{0.8}MA_{0.2}PbI₃ perovskite semiconductors. Absolute-value simulated 2D TIRV spectra for **c** MAPbI₃ and **d** FA_{0.8}MA_{0.2}PbI₃

The comparison of the measured spectra with the simple model calculations based on (9.12) and (9.13) allows a better insight into the frequencies of the phonons coupled with the N–H stretch oscillator. The experimental data for MA⁺ can be reproduced by assuming a coupling with the phonon mode centered at 32 cm⁻¹ (Fig. 9.10c). Reproducing the spectrum for FA⁺ requires out-of-phase coupling with the two-phonon modes, at 32 cm⁻¹ and 45 cm⁻¹, respectively (Fig. 9.10d). This simple analysis indicates that for both MA⁺ and FA⁺ the phonons coupled with the N–H stretch vibration are the octahedral distortion modes of the inorganic PB-I cage.

9.6 Outlook

The development of the two-dimensional optical spectroscopy techniques in the infrared and visible spectral ranges has allowed an insight into the couplings and correlations for nuclear and electronic degrees of freedom with frequencies above ~1000 cm⁻¹. This fresh and unique view proved to be highly fruitful and yielded improved models of structure and dynamics for a variety of systems in chemistry, biology and materials science. 2D TIRV spectroscopy enables the advantages of the 2D spectroscopy methods for the low-frequency, thermally particular relevant, energy range. The two systems considered in this chapter—water and perovskite semiconductor—demonstrate the use of this new tool in the research of materials as diverse as liquids and solids. The water study illustrates the application of 2D TIRV spectroscopy to investigate collective vibrations in complex samples which are composed of mixtures of distinct chemical substances—the problem that is particularly challenging to tackle using the far-infrared linear absorption spectroscopy. We believe that in the future, these unique capabilities will promote the use of 2D TIRV spectroscopy in a variety of research fields, enabling new exciting insights into the physical nature of the low-frequency molecular motions and their role in many types of physical and chemical phenomena.

References

1. M. Karplus, T. Ichiye, B.M. Pettitt, *Biophys. J.* **52**, 1083 (1987)
2. J. Guo, H.-X. Zhou, *Chem. Rev.* **116**, 6503 (2016)
3. H.N. Motlagh, J.O. Wrabl, J. Li, V.J. Hilser, *Nature* **508**, 331 (2014)
4. P.L. Geissler, C. Dellago, D. Chandler, J. Hutter, M. Parrinello, *Science* **291**, 2121 (2001)
5. D.F. Plusquellic, K. Siegrist, E.J. Heilweil, O. Esenturk, *ChemPhysChem* **8**, 2412 (2007)
6. P. Hamm, M. Zanni, *Concepts and Methods of 2D Infrared Spectroscopy* (Cambridge University Press, Cambridge, 2011)
7. W. Zhao, J. Wright, *Phys. Rev. Lett.* **83**, 1950 (1999)
8. W. Zhao, J.C. Wright, *Phys. Rev. Lett.* **84**, 1411 (2000)
9. K. Kwak, S. Cha, M. Cho, J.C. Wright, *J. Chem. Phys.* **117**, 5675 (2002)
10. F. D'Angelo, Z. Mics, M. Bonn, D. Turchinovich, *Opt. Express* **22**, 12475 (2014)
11. H.G. Roskos, M.D. Thomson, M. Krefß, T. Löffler, *Laser Photonics Rev.* **1**, 349 (2007)

12. J. Dai, J. Liu, X.-C. Zhang, *IEEE J. Sel. Top. Quantum Electron* **17**, 183 (2011)
13. S. Mukamel, *Principles of Nonlinear Optical Spectroscopy* (Oxford University Press, Oxford, 1995)
14. M. Cho, *Phys. Rev. A* **61**, 023406 (2000)
15. E.T.J. Nibbering, T. Elsaesser, *Chem. Rev.* **104**, 1887 (2004)
16. F. Perakis, L. De Marco, A. Shalit, F. Tang, Z.R. Kann, T.D. Kühne, R. Torre, M. Bonn, Y. Nagata, *Chem. Rev.* **116**, 7590 (2016)
17. S. Woutersen, U. Emmerichs, H.J. Bakker, *Science* **278**, 658 (1997)
18. C.J. Fecko, J.D. Eaves, J.J. Loparo, A. Tokmakoff, P.L. Geissler, *Science* **301**, 1698 (2003)
19. A. Luzar, D. Chandler, *Nature* **379**, 55 (1996)
20. B. Auer, R. Kumar, J.R. Schmidt, J.L. Skinner, *Proc. Natl. Acad. Sci.* **104**, 14215 (2007)
21. B.M. Auer, J.L. Skinner, *J. Chem. Phys.* **128**, 224511 (2008)
22. K. Ramasesha, L. De Marco, A. Mandal, A. Tokmakoff, *Nat. Chem.* **5**, 935 (2013)
23. S.M. Craig, F.S. Menges, C.H. Duong, J.K. Denton, L.R. Madison, A.B. McCoy, M.A. Johnson, *Proc. Natl. Acad. Sci.* **114**, E4706 (2017)
24. J.A. Fournier, W.B. Carpenter, N.H.C. Lewis, A. Tokmakoff, *Nat. Chem.* **10**, 932 (2018)
25. M. Grechko, T. Hasegawa, F. D'Angelo, H. Ito, D. Turchinovich, Y. Nagata, M. Bonn, *Nat. Commun.* **9**, 885 (2018)
26. L.M. Herz, *J. Phys. Chem. Lett.* **9**, 6853 (2018)
27. A.M.A. Leguy, A.R. Goñi, J.M. Frost, J. Skelton, F. Brivio, X. Rodríguez-Martínez, O.J. Weber, A. Pallipurath, M.I. Alonso, M. Campoy-Quiles, M.T. Weller, J. Nelson, A. Walsh, P.R.F. Barnes, *Phys. Chem. Chem. Phys.* **18**, 27051 (2016)
28. F. Brivio, J.M. Frost, J.M. Skelton, A.J. Jackson, O.J. Weber, M.T. Weller, A.R. Goñi, A.M.A. Leguy, P.R.F. Barnes, A. Walsh, *Phys. Rev. B* **92**, 144308 (2015)
29. H. Kim, J. Hunger, E. Cánovas, M. Karakus, Z. Mics, M. Grechko, D. Turchinovich, S.H. Parekh, M. Bonn, *Nat. Commun.* **8**, 687 (2017)
30. M. Grechko, S.A. Bretschneider, L. Vietze, H. Kim, M. Bonn, *Angew. Chemie Int. Ed.* **57**, 13657 (2018)